Dynamic Model With Slip for Wheeled Omnidirectional Robots

Robert L. Williams, II, *Member, IEEE*, Brian E. Carter, Paolo Gallina, and Giulio Rosati

***Abstract*—A dynamic model is presented for omnidirectional wheeled mobile robots, including wheel/motion surface slip. We derive the dynamics model, experimentally measure friction coefficients, and measure the force to cause slip (to validate our friction model). Dynamic simulation examples are presented to demonstrate omnidirectional motion with slip. After developing an improved friction model, compared to our initial model, the simulation results agree well with experimentally-measured trajectory data with slip. Initially, we thought that only high robot velocity and acceleration governed the resulting slipping motion. However, we learned that the rigid material existing in the discontinuities between omnidirectional wheel rollers plays an equally important role in determining omnidirectional mobile robot dynamic slip motion, even at low rates and accelerations.**

***Index Terms*—Dynamic model, omnidirectional mobile robot, sliding friction model, wheel slip.**

I. Introduction

RESEARCH interest in mobile robots has been tremendous in the past few years, as evidenced by review articles (e.g., [1], [2]).

Some researchers have considered slipping motion between the wheels and motion surface in mobile robots and vehicles. Choi and Sreenivasan have designed articulated wheeled vehicles with variable-length axles to eliminate kinematic wheel-surface slipping [3]. Hamdy and Badreddin developed a tenth-order nonlinear dynamic model for a wheeled mobile robot that includes slip between the driven wheels and the ground [4]. Rajagopalan developed an expression for the angular velocity of wheel slip for wheeled mobile robots with different combinations of steering and driving wheels, considering kinematics only [5]. Shekhar derives a dynamic model for mobile robots with wheel slip using accessibility and controllability in nonlinear control theory [6]. Balakrishna and Ghosal present a traction model accounting for slip in nonholonomic wheeled mobile robots [7]. Scheding *et al.* present experimental evaluation of a navigation system that handles autonomous vehicle wheel slip via multi-sensor feedback [8].

Several research groups are developing omnidirectional mobile robots and vehicles due to inherent agility benefits. Jung *et al.* developed an omnidirectional mobile robot base for the RoboCup competition [9]. RoboCup (www.robocup.org) is an international competition wherein teams of autonomous mobile robots compete in the game of soccer. Moore *et al.* present a control algorithm for an omnidirectional six-wheeled vehicle; each wheel is steered and driven independently [10]. Watanabe *et al.* present a controller for an autonomous omnidirectional mobile robot for service applications [11]. Witus investigates the mobility of a 6-wheeled omnidirectional vehicle with tire inflation control [12].

A recent article in these transactions presented a clever design plus experimental results for a spherical rolling robot [13]. However, this mobile robot is not omnidirectional and a no-slip condition was assumed. Our literature search revealed only two papers which mentioned slip in omnidirectional wheeled robots. Mori *et al.* claim that their vehicle avoids tire slippage by design since their omnidirectional motion base decouples steering and driving [14]. Dickerson and Lapin present a controller for omnidirectional Mecanum-wheeled vehicles, that includes wheel slip detection and compensation [15].

This paper presents a dynamic model for omnidirectional mobile robots that includes slipping between the wheels and the motion surface. The paper was motivated by a need in the Ohio University (Athens, OH) cross-disciplinary RoboCup team. In preliminary hardware testing of our omnidirectional three-wheeled player robot, significant slipping occurred which necessitated development of a dynamic model with slip. Though our work is motivated by RoboCup, the result is a general dynamic model for omnidirectional wheeled vehicles including slip. Our model includes both friction in the wheel rolling direction and in the transverse direction (normal to the first). One important issue turned out to be differing frictional characteristics due to the rigid material discontinuities between rollers in the omnidirectional wheels.

This paper does not focus on real-time control since our objective was to model and understand the sliding dynamics problem in simulation and experimentally. Based on our dynamic model, we will develop real-time control in the future, including a means to measure the slipping for feedback control.

This paper first presents our omnidirectional robot design, followed by dynamic modeling, including slip, a method to experimentally determine the coefficients of friction and validate our friction model, and simulation and experimental results to demonstrate omnidirectional robot dynamics considering slip.

Manuscript received May 11, 2001; revised November 27, 2001. This paper was recommended for publication by Associate Editor R. Simmons and Editor I. Walker upon evaluation of the reviewers' comments.

R. L. Williams, II, is with the Department of Mechanical Engineering, Ohio University, Athens, OH 45701 USA (e-mail: williar4@ohio.edu).

B. E. Carter was with Ohio University, Athens, OH 45701 USA. He is now with Automation Tooling Systems, Inc., Westerville, OH 43081 USA (e-mail: brian_carter@ats-ohio.com).

P. Gallina was with Ohio University, Athens, OH 45701 USA, on leave from the University of Padova, 1–I 35131 Padova, Italy. He is now with the Department of Energetics, University of Trieste, 1–I 34127 Trieste, Italy (e-mail: paolo.gallina@unipd.it).

G. Rosati is with the Department of Innovation in Mechanics and Management, University of Padova, 1–I 35131 Padova, Italy (e-mail: giulio.rosati@unipd.it).

Publisher Item Identifier S 1042-296X(02)05178-9.

1042-296X/02$17.00 © 2002 IEEE

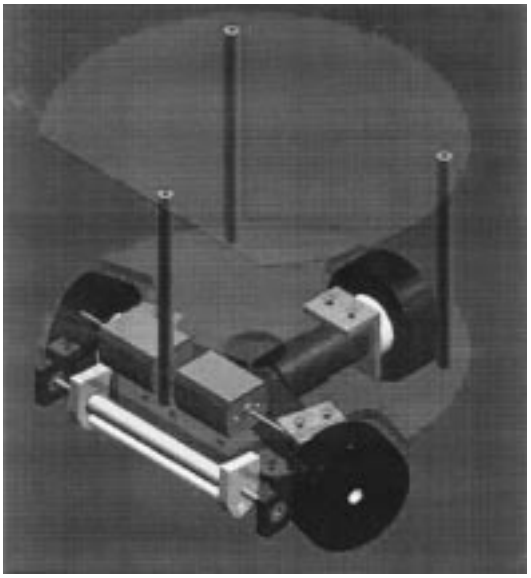

Fig. 1. CAD model.

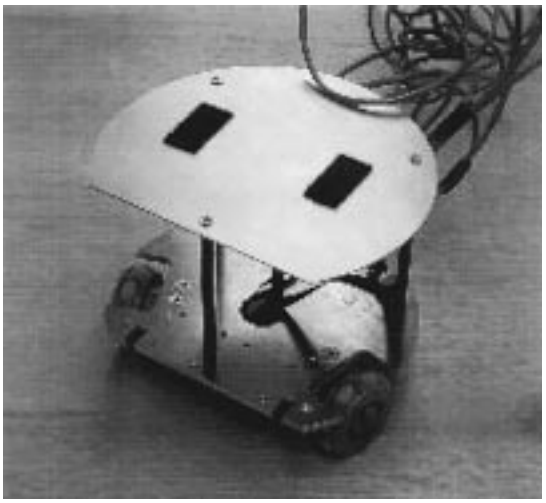

Fig. 2. Hardware photo.

II. Omnidirectional Robot Model

In early evaluation of our three-wheeled omnidirectional mobile robot hardware, slipping was encountered between the wheels and the carpet playing field when the robot was in motion. This unexpected behavior motivated the development of a dynamic model including slip. This model is presented in the next section; the current section describes the omnidirectional robot hardware and model.

Fig. 1 shows the CAD model for the three-wheeled omnidirectional mobile robot and Fig. 2 shows a photograph of the prototype hardware.

Fig. 3 shows the top view of our general three-wheeled omnidirectional mobile robot model. The variables, used in the dynamic model of the next section, are explained below.

The inertially fixed frame is $\{0\}$ and the moving Cartesian reference frame is $\{M\}$. The rear wheel is aligned in the X_M direction, and the front two wheels are symmetrically placed, aligned by constant angle δ from the Y_M axis (shown only for the left wheel in Fig. 3). We assume the center of mass for the

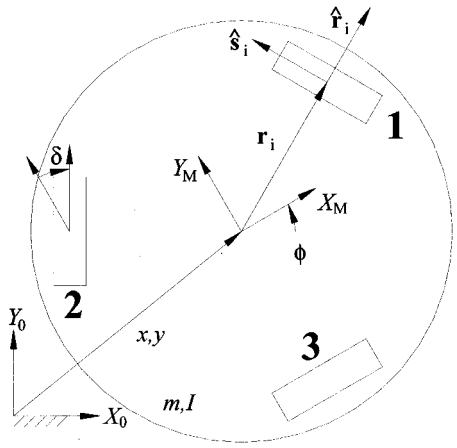

Fig. 3. omnidirectional robot model, top view.

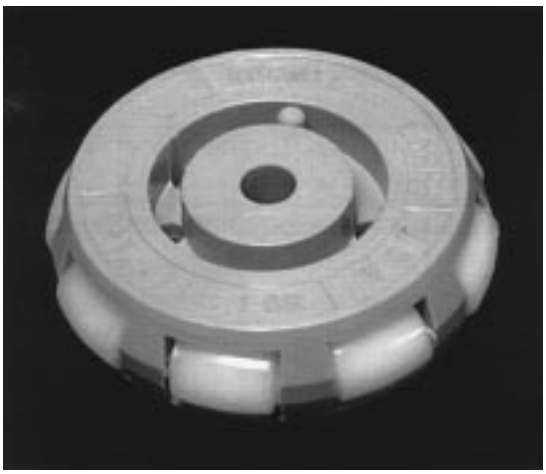

Fig. 4. Commercial wheel.

robot is located at the center of the robot circle, which is the origin of $\{M\}$. This was one of our guiding principles in design. The robot mass is m and the robot mass moment of inertia about the Z_M axis through the center of mass is I. Each wheel center position is given by position vector $\mathbf{r}_i$, from the origin of $\{M\}$ to the center of the wheel. The unit vector $\hat{\mathbf{r}}_i$ in this direction is also the direction of each wheel's angular velocity vector (i.e., $\hat{\mathbf{r}}_i$ is the axle direction). The unit vector $\hat{\mathbf{s}}_i$ is normal to $\hat{\mathbf{r}}_i$, giving the instantaneous direction of each wheel. The Cartesian variables for omnidirectional motion are $\mathbf{X} = \{x \quad y \quad \phi\}^T$. As seen in Fig. 3, the translational vector giving the position of the origin of $\{M\}$, with respect to the origin of $\{0\}$, is $\{x \quad y\}^T$ (expressed in the coordinates of $\{0\}$). Also, the angle ϕ gives the orientation of the robot with respect to the inertial frame horizontal direction X_0.

The omnidirectional motion is enabled via special wheels. Fig. 4 shows a commercial omnidirectional wheel (kornylak.com) used in our mobile robot designs. It is important to note that these wheels were not intended for omnidirectional mobile robots; rather, they were developed for material-handling applications. For a good discussion on omnidirectional wheels for mobile robots, see [16]. Our application dictated economical, commercially available wheels, which led to our choice of wheel.

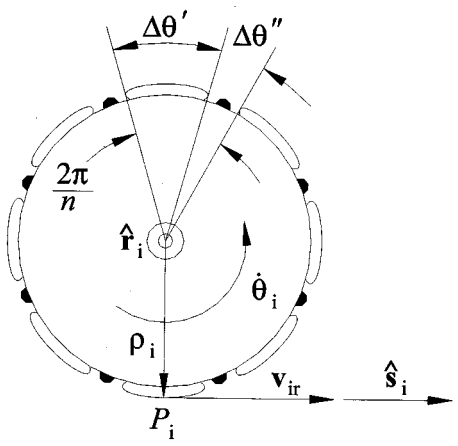

Fig. 5. Wheel detail.

As seen in Fig. 4, the axle is mounted normal to the wheel's circle as in a standard wheel. However, the contact with the ground is via rollers that are free to spin about an axis in-line with the circle circumference, normal to the wheel axle. This enables omnidirectional motion.

III. Omnidirectional Robot Dynamics Modeling

This section presents omnidirectional mobile robot modeling with slip included between the wheels and motion surface. Section III-A presents the model, plus the friction model and experimental measurement of the friction coefficients. Section III-B presents a method to experimentally validate our theoretical friction model and measured friction coefficients.

A. Dynamics Model with Slip

The dynamics model is developed in this section for a three-wheeled omnidirectional robot, but it applies to any omnidirectional robot with three or more wheels. The dynamic model is shown in the top view of Fig. 3 above, and is described in Section II. Fig. 5 shows modeling details for the ith wheel from a side view. Fig. 5 shows that our omnidirectional wheel contains $n = 8$ rollers; further, the fixed angle $\Delta\theta'$ covers each roller sector, and the fixed angle $\Delta\theta''$ covers each sector between rollers.

As seen in Fig. 5, we denote P_i ($i = 1, 2, 3$) as the contact point between the ith wheel and the ground. Instantaneously, P_i belongs to the ground and the wheel, but we consider that P_i is on the wheel. The velocity vector $\mathbf{v}_i$ for point P_i is

$$\mathbf{v}_i = \mathbf{v}_G + \boldsymbol{\omega} \times \mathbf{r}_i + \mathbf{v}_{ir}. \tag{1}$$

$\mathbf{v}_G$ is the vehicle center of mass translational velocity, $\boldsymbol{\omega}$ is the vehicle rotational velocity. Both translational and rotational velocity vectors are expressed with respect to the inertially-fixed frame $\{0\}$. $\mathbf{r}_i$ is the position vector giving the wheel center position with respect to the moving frame $\{M\}$, expressed in the inertial frame, and $\mathbf{v}_{ir}$ is the peripheral wheel speed with respect to the moving frame, expressed in the inertial frame. Note that when $\mathbf{v}_i$ is null, there is no slipping motion.

We can express $\mathbf{v}_{ir}$ as a function of the wheel angular velocity vector $\dot{\boldsymbol{\theta}}_i$ and the wheel radius vector $\boldsymbol{\rho}_i$

$$\mathbf{v}_{ir} = \dot{\boldsymbol{\theta}}_i \times \boldsymbol{\rho}_i. \tag{2}$$

The wheel angular velocity vector $\dot{\boldsymbol{\theta}}_i = \dot{\theta}_i \hat{\mathbf{r}}_i$ is the scalar wheel speed $\dot{\theta}_i$ in the unit $\hat{\mathbf{r}}_i$ direction, and the wheel radius position vector $\boldsymbol{\rho}_i$ is the scalar wheel radius ρ_i from the wheel center to point P_i. Note the result of (2) is scalar $\rho_i \dot{\theta}_i$ in the unit wheel direction $\hat{\mathbf{s}}_i$ (normal to $\hat{\mathbf{r}}_i$). The next two sections present our initial friction model and experimental measurement of friction coefficients.

1) Initial Friction Model: There are two directions of wheel/ground friction to consider. The first is friction in the direction of the wheel rotation, $\hat{\mathbf{s}}_i$, and the second is transverse to this direction, $\hat{\mathbf{r}}_i$. Initially, our model only included the former case, but initial trials with the omnidirectional motion base hardware indicated that we must also include the latter friction case.

For use with friction in the direction of the wheel rotation, the sliding velocity component v_{Wi} in the ith wheel is obtained by dotting the total point P_i velocity from (1) into the $\hat{\mathbf{s}}_i$ unit direction

$$v_{Wi} = \mathbf{v}_i \bullet \hat{\mathbf{s}}_i = \mathbf{v}_G \bullet \hat{\mathbf{s}}_i + (\omega \times \mathbf{r}_i) \bullet \hat{\mathbf{s}}_i + \rho_i \dot{\theta}_i. \tag{3}$$

To convert wheel positions and unit directions in the moving frame $\{M\}$ ($^M\mathbf{r}_i$ and $^M\hat{\mathbf{s}}_i$) to the inertial frame $\{0\}$ ($\mathbf{r}_i$ and $\hat{\mathbf{s}}_i$), use (4)

$$\hat{\mathbf{s}}_i = {}^0_M\mathbf{R}\,{}^M\hat{\mathbf{s}}_i \quad \mathbf{r}_i = {}^0_M\mathbf{R}\,{}^M\mathbf{r}_i. \tag{4}$$

${}^0_M\mathbf{R}$ is the orthonormal rotation matrix giving the orientation of the moving frame $\{M\}$ with respect to the inertial frame $\{0\}$

$${}^0_M\mathbf{R} = \begin{bmatrix} \cos\phi & -\sin\phi \\ \sin\phi & \cos\phi \end{bmatrix}. \tag{5}$$

Therefore, (3) becomes

$$v_{Wi} = \mathbf{v}_G \bullet {}^0_M\mathbf{R}\,{}^M\hat{\mathbf{s}}_i + \left(\omega \times {}^0_M\mathbf{R}\,{}^M\mathbf{r}_i\right) \bullet {}^0_M\mathbf{R}\,{}^M\hat{\mathbf{s}}_i + \rho_i \dot{\theta}_i. \tag{6}$$

On the other hand, the transverse sliding velocity component v_{Ti} in the ith wheel, along the wheel axle direction $\hat{\mathbf{r}}_i$ is

$$v_{Ti} = \mathbf{v}_G \bullet {}^0_M\mathbf{R}\,{}^M\hat{\mathbf{r}}_i + \left(\omega \times {}^0_M\mathbf{R}\,{}^M\mathbf{r}_i\right) \bullet {}^0_M\mathbf{R}\,{}^M\hat{\mathbf{r}}_i. \tag{7}$$

If we assume the vehicle weight is equally distributed on each wheel, the friction force exerted on wheel i by the motion surface through point P_i is given by

$$\mathbf{F}_i = -\frac{mg}{3}\left(\mu_W(v_{Wi})\,{}^0_M\mathbf{R}\,{}^M\hat{\mathbf{s}}_i + \mu_T(v_{Ti})\,{}^0_M\mathbf{R}\,{}^M\hat{\mathbf{r}}_i\right) \tag{8}$$

where $\mu_W(\cdot)$ is a function representing the friction coefficient versus the sliding velocity in the direction of the wheel rotation, and $\mu_T(\cdot)$ is the friction coefficient for the transverse wheel direction.

The dynamic equations are

$$m\ddot{x} = \sum_{i=1}^{3} \hat{\mathbf{x}} \bullet \mathbf{F}_i \quad m\ddot{y} = \sum_{i=1}^{3} \hat{\mathbf{y}} \bullet \mathbf{F}_i \quad I\ddot{\phi} = \sum_{i=1}^{3} \hat{\mathbf{z}} \bullet (\mathbf{r}_i \times \mathbf{F}_i) \tag{9}$$

where $\hat{\mathbf{x}}$, $\hat{\mathbf{y}}$, $\hat{\mathbf{z}}$ are the unit direction vectors of the inertial frame. The nonlinear dynamic equations are of the form $\ddot{\mathbf{X}} = \mathbf{f}\left(\mathbf{X}, \dot{\mathbf{X}}\right)$ as in (10), shown at the bottom of the next page.

In our simulation we use the following simplified formulas for coefficient of friction:

$$\mu_W(v_W) = \mu_{W\max}\tfrac{2}{\pi}\mathrm{atan}(kv_W)$$
$$\mu_T(v_T) = \mu_{T\max}\tfrac{2}{\pi}\mathrm{atan}(kv_T) \tag{11}$$

where $\mu_{W\max}$, $\mu_{T\max}$, and k are constants, and v_W and v_T are the sliding velocity magnitudes in the wheel rotation and transverse directions, respectively.

Notice that in our friction model, the dynamic friction coefficient is assumed to be constant and equal to the constant static friction coefficient; we assume that this simplified model will be sufficient to match experimental results. Equation (11) are artificial functions to conveniently represent the friction coefficients stably in simulation, avoiding algorithmic problems that may arise when using a discontinuous function at zero sliding velocity. This is a common approach; for an example, see [17], which presents a parametric model and experimental results for tire–road friction coefficients for automotive applications with different road conditions. The k constant governs the steepness of the change between positive and negative $\mu_{W\max}$ and $\mu_{T\max}$ about zero sliding velocity. We chose $k = 1000$ by eye and to ensure numerical stability in Simulink. Note that (11) defines positive friction coefficient to correspond with positive sliding velocity. The opposite sign behavior (Coulomb friction acts opposite to the sliding direction) is taken into account in (8). Also, $\mu_{T\max}$ is much less than $\mu_{W\max}$ due to the design of the omnidirectional wheels used, with smaller friction in the transverse direction than the primary driving direction, owing to the passive rolling cylinders (see Fig. 4).

Our simple friction model is intended to capture gross real-world friction characteristics. Improvements are certainly possible by considering stiction and different coefficients for the static and dynamic friction coefficients. For an improved friction model, see [18]; these authors present a tire–road friction model using the LuGre dry friction model and including tire dynamics. Our wheel and rolling surface materials are not similar to the tire–road problem.

2) Experimental Friction Coefficient Measurement: We measured experimental values for $\mu_{W\max}$ and $\mu_{T\max}$ for use in the dynamic simulation, for two motion surfaces: paper and carpet. In order to estimate $\mu_{W\max}$, we built a special vehicle in which all the wheels were aligned along a common direction. Each wheel angle was fixed in such a way that only the rollers were in contact with the motion surface. The surface was made up of a rigid board covered with paper or carpet. The square board was pivoted on one edge. The vehicle was placed so that all wheel axes were parallel to the pivoting edge. Then we gradually lifted the board until the special vehicle slid. $\mu_{W\max}$was determined as the tangent of the angle between the lifted board and the horizontal plane. To measure $\mu_{T\max}$, we repeated the above procedure, placing the special vehicle so that all wheel axes were perpendicular to the pivoting edge. Again, only the rollers were in contact with the motion surface. The results are $\mu_{W\max} = 0.26$ and $\mu_{T\max} = 0.09$ for the paper motion surface, and $\mu_{W\max} = 0.25$ and $\mu_{T\max} = 0.15$ for the carpet motion surface.

These results were averaged over several trials. For each surface, the transverse roller friction ($\mu_{T\max}$) is much smaller than that in the wheel rotation direction ($\mu_{W\max}$). The wheel rotation direction friction coefficients are nearly the same for paper and carpet.

B. Initial Simulation and Experimental Results

This section presents simulated and experimental results to demonstrate omnidirectional mobile robot motion considering slip. Simulation results are presented first using the initial friction model; next, the experimental procedure and results are presented and compared with the simulation results.

For both of the following sections (simulation and experimental results), the same motion condition is used. We command straight-line motion from initial point $\mathbf{X}_0 = \{0.0 \quad 0.0 \quad 0\}^T$ to final point $\mathbf{X}_F = \{0.4 \quad 0.0 \quad 0\}^T$ (m) in a specified time of $t_F = 3.5$ s. We consider only X motion since, due to robot symmetry, Y motion is inherently less affected by slip. ϕ motion could have significant slip behavior; this will be the subject of future experimental work. Fig. 3 shows our robot hardware geometry (our design has $\delta = 15°$. We were driven to this choice by RoboCup size constraints; $\delta = 30°$ is preferable for robot symmetry.). The motion is commanded in the inertial frame, $\{0\}$ in Fig. 3. Robot orientation ϕ is also important in slip dynamics, but the pure X motion will also demonstrate (unwanted) orientation slip motion. Robot orientation is commanded as zero for the motion example.

Since we wish to demonstrate slipping, we make no attempt to smooth the commanded velocity motion from rest or ending at rest. Hence, the simulated commanded wheel acceleration is infinite at the start, and the deceleration is infinite at the end of the time period. Of course, neither the real or simulated robot can achieve infinite acceleration or deceleration, but the high accelerations at the start and end are sufficient to cause slip. Constant velocity is commanded in between the start and end. Clearly, for omnidirectional mobile robot applications we need

$$\begin{Bmatrix} \ddot{x} \\ \ddot{y} \\ \ddot{\phi} \end{Bmatrix} = \begin{Bmatrix} -\dfrac{g}{3}\displaystyle\sum_{i=1}^{3} \hat{\mathbf{x}} \bullet \left(\mu_W(v_{Wi}) {}^0_M\mathbf{R}^M \hat{\mathbf{s}}_i + \mu_T(v_{Ti}) {}^0_M\mathbf{R}^M \hat{\mathbf{r}}_i\right) \\ -\dfrac{g}{3}\displaystyle\sum_{i=1}^{3} \hat{\mathbf{y}} \bullet \left(\mu_W(v_{Wi}) {}^0_M\mathbf{R}^M \hat{\mathbf{s}}_i + \mu_T(v_{Ti}) {}^0_M\mathbf{R}^M \hat{\mathbf{r}}_i\right) \\ -\dfrac{mg}{3I}\displaystyle\sum_{i=1}^{3} \hat{\mathbf{z}} \bullet \left[{}^0_M\mathbf{R}^M \mathbf{r}_i \times \left(\mu_W(v_{Wi}) {}^0_M\mathbf{R}^M \hat{\mathbf{s}}_i + \mu_T(v_{Ti}) {}^0_M\mathbf{R}^M \hat{\mathbf{r}}_i\right)\right] \end{Bmatrix}. \tag{10}$$

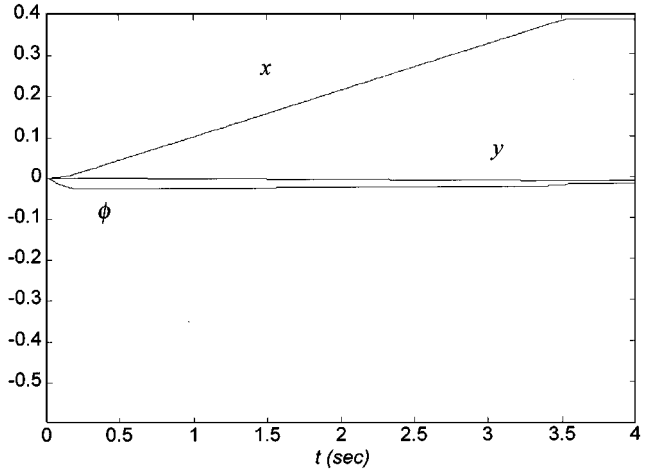

(a)

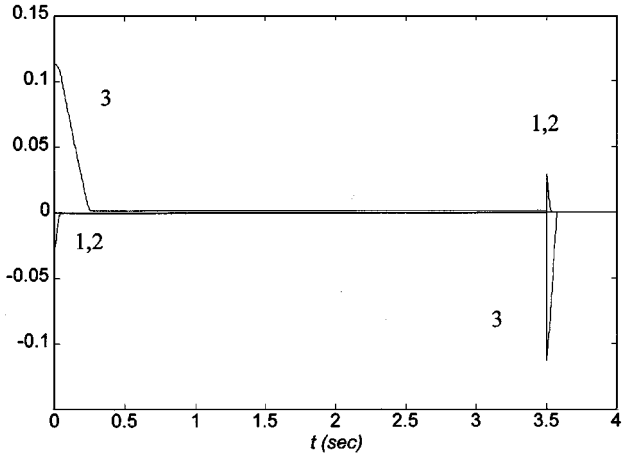

(b)

Fig. 6. (a) Cartesian displacements (m and rad). (b) Wheel sliding speeds v_{W1}, v_{W2}, v_{W3} (m/s).

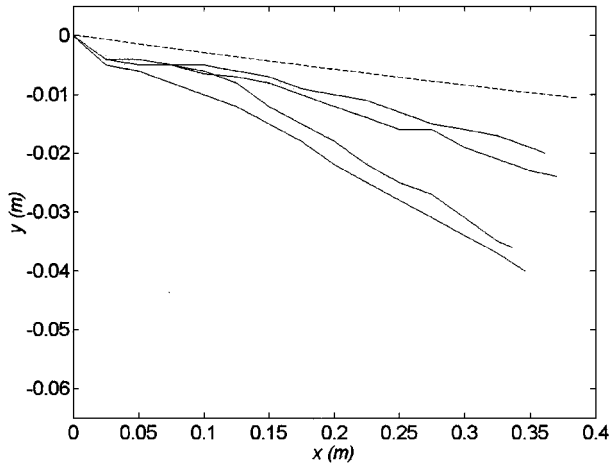

(a)

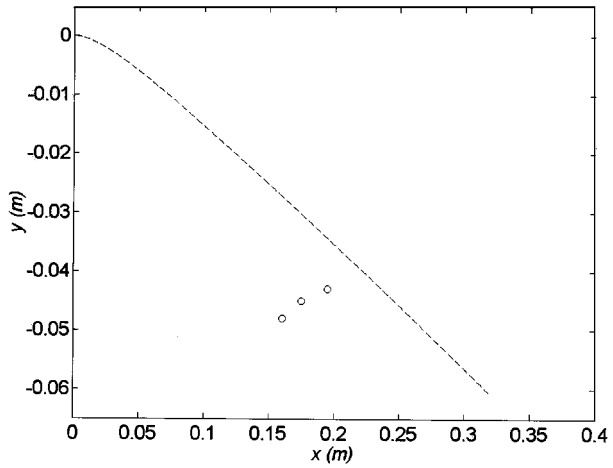

(b)

Fig. 7. (a) Simulated (dashed) and experimental (solid) results for paper motion surface. (b) Simulated (dashed) and experimental (O) results for carpet motion surface.

smoother trajectory generation, perhaps using fifth-order polynomials for wheel displacements.

For this motion example, the required constant wheel angular speeds are $\dot{\theta}_1 = \dot{\theta}_2 = +1.16$ and $\dot{\theta}_3 = -4.50$ (rad/s); note the wheel numbering convention is given in Fig. 3. With this motion example, we consider two motion surfaces to include different levels of friction: a smooth paper surface and a rough carpet surface. The experimentally-measured friction coefficients for use in simulation were presented in Section III-A2.

1) Initial Simulation Results: We developed a Matlab Simulink model to simulate omnidirectional mobile robot dynamic motion considering slip. In this section, we present simulated dynamics results using the initial friction model of Section III-A1. The simulated motion condition, surfaces, and friction coefficients are described above. To save space, we only show the simulated case with the paper motion surface.

Fig. 6(a) shows the Cartesian displacements, and Fig. 6(b) shows the associated sliding speeds in the wheel directions for each wheel, for the simulated motion. In Fig. 6(b), the simulated sliding speeds for wheels one and two are identical due to symmetry. As seen in Fig. 6(b), slipping is encountered at the start and end of motion, due to the infinite commanded acceleration and deceleration, but not in the middle. The effect, seen in Fig. 6(a), is that x falls short of its goal of 0.4 m by 14mm, while y drifts -9 mm from the desired zero. ϕ drifts from its commanded value of zero by -0.016 rad at the end; in the middle of motion, the ϕ drift is larger. From approximately $t = 0.25$ s to $t = t_F = 3.5$ s, the x motion is linear, which means constant velocity has been achieved and the simulation predicts no unwanted slipping in this range.

2) Experimental Procedure and Results: Experiments were performed to validate the results of our simulation work, using both paper and carpet motion surfaces. Our mobile robot was tethered for the experiments. Eventually, our mobile robots will be free, the on-board PCs communicating with the host PC via wireless Ethernet. To control the robot during the experimental trials, WinCon 3.1 in conjunction with Simulink was used. This enabled us to use a Quanser Multi-Q3 board to control the motor angular velocities through a feedback loop. The experimental robot was shown earlier in Fig. 2. Please note that the robot cables must be held manually to avoid constraining the robot motion. Experimental trajectories for the paper surface were traced by attaching a lightweight pencil to the robot center of mass. This was not feasible for the carpet surface, so only the end points and final orientations were recorded in the carpet cases.

Another way to present the simulation result from Fig. 6(a) is given in Fig. 7(a) and (b), plotting y versus x for the paper and

carpet motion surfaces. The experimental data are included for comparison.

In Fig. 7(a), the dashed curve is the simulated result using the initial friction model with the paper motion surface; this curve was obtained by plotting y versus x (rather than versus time t) from Fig. 6(a). The four solid curves are the results of the four experimental trials for the same motion case, with the paper motion surface. In Fig. 7(b), the three single **O** points are the ending points for the three experimental trials with the carpet motion surface (these cases also tried to obtain pure X motion from 0 to 0.4 m; no trajectory is available, as explained above). The dashed curve is the simulated result using the initial friction model and the carpet motion surface (not previously shown).

IV. Improved Model

Clearly, from Fig. 7, the initial simulation results do not agree well with the experimental results, when using the initial friction model with either motion surface, paper or carpet. This poor result motivated the need for an improved friction model. We use the same type of simple friction model, but augmented for the special nature of our omnidirectional wheels' geometry. This section presents our improved friction model, validation of our friction coefficient measurements, and improved simulation results, compared with the preceding experimental results.

A. Improved Friction Model

We noticed that, for our choice of wheel, the friction coefficient is a function of the wheel angle θ_i. When the rigid wheel material between two rollers is in contact with the motion surface (see Fig. 5), the friction coefficients change. This undesirable behavior cannot be blamed on the wheel manufacturer, since the wheels were not made for use in omnidirectional mobile robots. We account for this phenomenon by introducing nonlinear friction coefficients as a function of the sliding speeds *and* wheel angle. Let n be the number of rollers in the wheel ($n = 8$ in Figs. 4 and 5). Each roller and rigid portion is within angular sector $2\pi/n$. Each sector can be split into two different (roller and rigid) portions with different friction coefficients; $\Delta\theta' + \Delta\theta'' = 2\pi/n$ as seen in Fig. 5. Therefore, we have different friction coefficients according to which part of the sector is in contact with the motion surface at a given time. In our hardware wheel, $\Delta\theta'$ (the roller) accounts for 90% of each angular sector $2\pi/n$, and $\Delta\theta''$ (the rigid material) accounts for 10%.

To summarize, our improved friction model is the same as (11), but we use roller values for friction coefficient ($\mu'_{W\max}$ and $\mu'_{T\max}$) when the wheel angle is within the $\Delta\theta'$ sector and we use rigid material values ($\mu''_{W\max}$ and $\mu''_{T\max}$) when the wheel angle is within $\Delta\theta''$.

We measured experimental values for $\mu'_{W\max}$, $\mu'_{T\max}$, $\mu''_{W\max}$, and $\mu''_{T\max}$ for both paper and carpet motion surfaces. $\mu'_{W\max}$ and $\mu''_{T\max}$ were already measured in Section III-A2; now we have added a single prime superscript to indicate roller. $\mu''_{W\max}$ and $\mu''_{T\max}$ were measured in the same way, but in these cases the wheel angle was fixed so that only the wheel sector between two consecutive rollers was in contact with the motion surface. The double-prime superscript indicates the rigid material between rollers. The results, averaged over several trials, are shown in Table I (the first two columns are the same as the previous results in Section III-A2). Again, for each surface, the transverse roller friction ($\mu'_{T\max}$) is much smaller than that in the wheel rotation direction ($\mu'_{W\max}$). The wheel rotation direction roller friction coefficients ($\mu'_{W\max}$) are nearly the same for paper and carpet. For the material between the rollers (double prime), the carpet friction coefficient value is higher than that of the paper surface. As expected, the wheel and transverse coefficients of friction ($\mu''_{W\max}$ and $\mu''_{T\max}$) are identical for the material between the rollers (for a given motion surface).

TABLE I
Experimental Friction Coefficients

Surface	$\mu'_{W\max}$	$\mu'_{T\max}$	$\mu''_{W\max}$	$\mu''_{T\max}$
Paper	0.26	0.09	0.47	0.47
Carpet	0.25	0.15	0.56	0.56

B. Validation of Friction Coefficient Measurements

In an attempt to validate both our experimental static friction coefficients and our improved friction model, we now derive and measure the maximum allowable force yielding static equilibrium for the omnidirectional robot. The friction force on each wheel i is

$$\mathbf{F}_i = F_{Wi}\hat{\mathbf{s}}_i + F_{Ti}\hat{\mathbf{r}}_i \tag{12}$$

where F_{Wi} and F_{Ti} are, respectively, the friction force magnitudes along the wheel motion direction and along the wheel axis direction (transverse). Suppose we apply an external force $\mathbf{F}_e = \{F_e \quad 0 \quad 0\}^T$ at the robot mass center. What is the maximum force $F_{e_{\max}}$ we can apply at the mass center and still maintain static equilibrium (avoid sliding motion)? The external force we apply is resisted by the friction forces and moment

$$\begin{aligned} F_e &= \sum_{i=1}^{3} \hat{s}_{ix} \cdot F_{Wi} + \sum_{i=1}^{3} \hat{r}_{ix} \cdot F_{Ti} \\ 0 &= \sum_{i=1}^{3} \hat{s}_{iy} F_{Wi} + \sum_{i=1}^{3} \hat{r}_{iy} F_{Ti} \\ 0 &= \sum_{i=1}^{3} (r_{ix}\hat{s}_{iy} - r_{iy}\hat{s}_{ix}) F_{Wi} + \sum_{i=1}^{3} (r_{ix}\hat{r}_{iy} - r_{iy}\hat{r}_{ix}) F_{Ti} \end{aligned} \tag{13}$$

which is rewritten as

$$\mathbf{F}_e = [\mathbf{A}_W \quad \mathbf{A}_T] \begin{Bmatrix} \mathbf{F}_W \\ \mathbf{F}_T \end{Bmatrix} \tag{14}$$

where

$$\mathbf{A}_W = \begin{bmatrix} \hat{s}_{1x} & \hat{s}_{2x} & \hat{s}_{3x} \\ \hat{s}_{1y} & \hat{s}_{2y} & \hat{s}_{3y} \\ r_{1x}\hat{s}_{1y} - r_{1y}\hat{s}_{1x} & r_{2x}\hat{s}_{2y} - r_{2y}\hat{s}_{2x} & r_{3x}\hat{s}_{3y} - r_{3y}\hat{s}_{3x} \end{bmatrix}$$

$$\mathbf{A}_T = \begin{bmatrix} \hat{r}_{1x} & \hat{r}_{2x} & \hat{r}_{3x} \\ \hat{r}_{1y} & \hat{r}_{2y} & \hat{r}_{3y} \\ r_{1x}\hat{r}_{1y} - r_{1y}\hat{r}_{1x} & r_{2x}\hat{r}_{2y} - r_{2y}\hat{r}_{2x} & r_{3x}\hat{r}_{3y} - r_{3y}\hat{r}_{3x} \end{bmatrix}$$

$$\mathbf{F}_W = \{F_{W1} \quad F_{W2} \quad F_{W3}\}^T$$

$$\mathbf{F}_T = \{F_{T1} \quad F_{T2} \quad F_{T3}\}^T.$$

Notice that the elements of $\mathbf{A}_W$, $\mathbf{A}_T$ are expressed in the inertial frame, so they are functions of robot orientation ϕ. We can express $\mathbf{A}_W$, $\mathbf{A}_T$ as a product of two matrices

$$\mathbf{A}_W = \mathbf{R}\mathbf{B}_W \quad \mathbf{A}_T = \mathbf{R}\mathbf{B}_T \tag{15}$$

where $\mathbf{B}_W$, $\mathbf{B}_T$ are identical to $\mathbf{A}_W$, $\mathbf{A}_T$, except all vector components are expressed in the moving frame $\{M\}$, and

$$\mathbf{R} = \begin{bmatrix} {}^0_M\mathbf{R} & \begin{matrix}0\\0\end{matrix} \\ \begin{matrix}0 & 0\end{matrix} & 1 \end{bmatrix} = \begin{bmatrix} c\phi & -s\phi & 0 \\ s\phi & c\phi & 0 \\ 0 & 0 & 1 \end{bmatrix}.$$

Notice that with this notation, $\mathbf{B}_W$, $\mathbf{B}_T$ are constant, while $\mathbf{R}$ is a function of the angular position. Therefore,

$$\mathbf{F}_e = \mathbf{R}[\mathbf{B}_W \quad \mathbf{B}_T] \begin{Bmatrix} \mathbf{F}_W \\ \mathbf{F}_T \end{Bmatrix}. \tag{16}$$

The set of friction forces that can be exerted by the motion surface contact point on the robot is given by

$$\Sigma_F = \left\{ \mathbf{F} \left| -\frac{mg}{3}\mu'_{W\max} \le F_{Wi} \le \frac{mg}{3}\mu'_{W\max}, \right. \right. \\ \left. \left. -\frac{mg}{3}\mu'_{T\max} \le F_{Ti} \le \frac{mg}{3}\mu'_{T\max} \right\} \tag{17}$$

where

$$\mathbf{F} = \begin{Bmatrix} \mathbf{F}_W \\ \mathbf{F}_T \end{Bmatrix} = \{ F_{W1} \quad F_{W2} \quad F_{W3} \quad F_{T1} \quad F_{T2} \quad F_{T3} \}^T.$$

Equation (17) represents the dominion of the linear transformation given by (16). The image of Σ_F is a polytope that represents the maximum force available along x, y, and ϕ. Our aim is to calculate the maximum value of F_e that satisfies (16) and, at the same time, belongs to the image of Σ_F. There are several standard ways to solve this problem using polytope theory [19]. For our particular problem we can turn the problem into a typical constrained maximization problem and solve it with numerical software like Mathematica.

If we split the matrix $\mathbf{R}[\mathbf{B}_W \quad \mathbf{B}_T]$ in two sub-matrices, we have

$$\begin{bmatrix} \mathbf{B}_1 \\ \mathbf{B}_2 \end{bmatrix} = \mathbf{R}[\mathbf{B}_W \quad \mathbf{B}_T] \qquad \begin{matrix} F_e = \mathbf{B}_1\mathbf{F} \\ 0 = \mathbf{B}_2\mathbf{F} \end{matrix} \tag{18}$$

therefore, $F_{e\max} = \max\{F_e | F_e = \mathbf{B}_1\mathbf{F}, 0 = \mathbf{B}_2\mathbf{F}, \mathbf{F} \in \Sigma_F\}$. Notice that $F_{e\max}$ is a function of ϕ.

Using $\mu'_{W\max}$ and $\mu'_{T\max}$ determined experimentally above, we can plot the maximum force before sliding, $F_{e\max}$, versus mobile robot orientation ϕ, using the theory of this section. $F_{e\max}$ can also be measured experimentally with the following procedure. When we apply an external force to the robot along the X direction, if the sum of the three friction force components along X is high enough, the robot does not move. We increase the external force until the robot moves. The minimum external force to move the robot is recorded as $F_{e\max}$. The procedure is repeated with different angular orientations ϕ. An experimental plot of $F_{e\max}$ versus ϕ is shown in Fig. 8. Note this figure gives results for the omnidirectional robot (Fig. 2 and Fig. 3), not the special vehicle constructed for friction coefficient measurement in Section III-A2 and Section IV-A. Due to robot symmetry, plotting results from 0 to $\pi/2$ rad in robot orientation is sufficient. Three series of data have been collected. Considering static conditions, the experimental data (O) and the theoretical result (solid curve, solved via Mathematica) compare reasonably well, which serves to validate both our friction coefficients and our friction model. Although the agreement is reasonable, the experimental repeatability is very low.

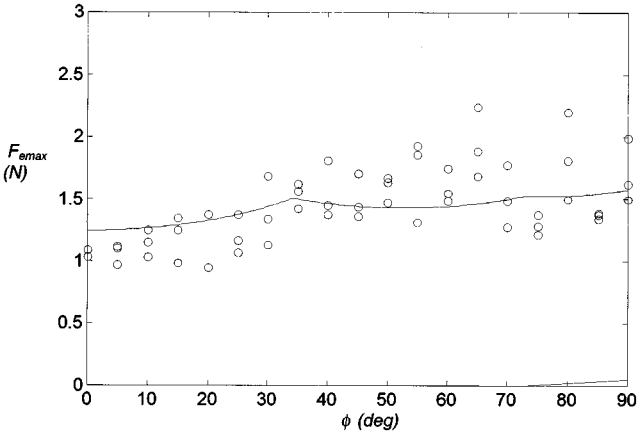

Fig. 8. Experimental (O) and theoretical (solid) $F_{e\max}$.

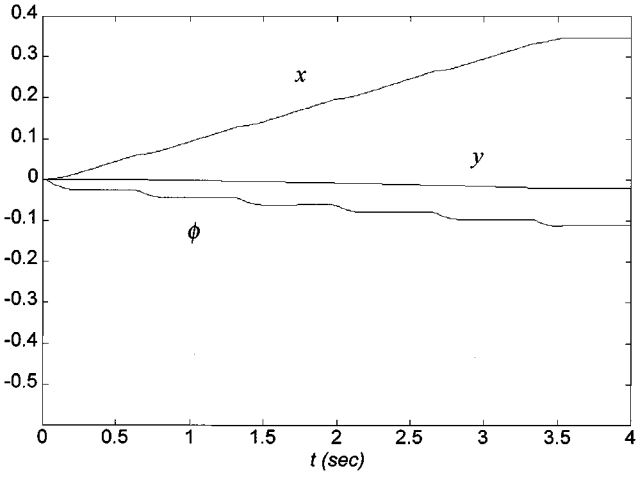

(a)

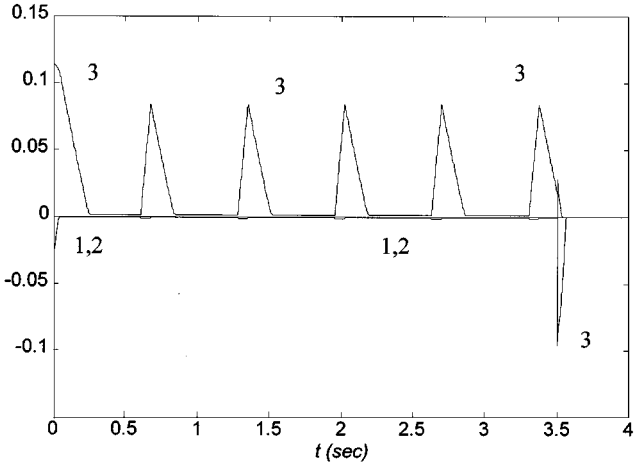

(b)

Fig. 9. (a) Cartesian displacements (m and rad). (b) Wheel sliding speeds v_{W1}, v_{W2}, v_{W3} (m/s).

C. Improved Simulation Results

In an attempt to improve the poor simulation/experimental agreement of Fig. 7, the improved friction model of this section

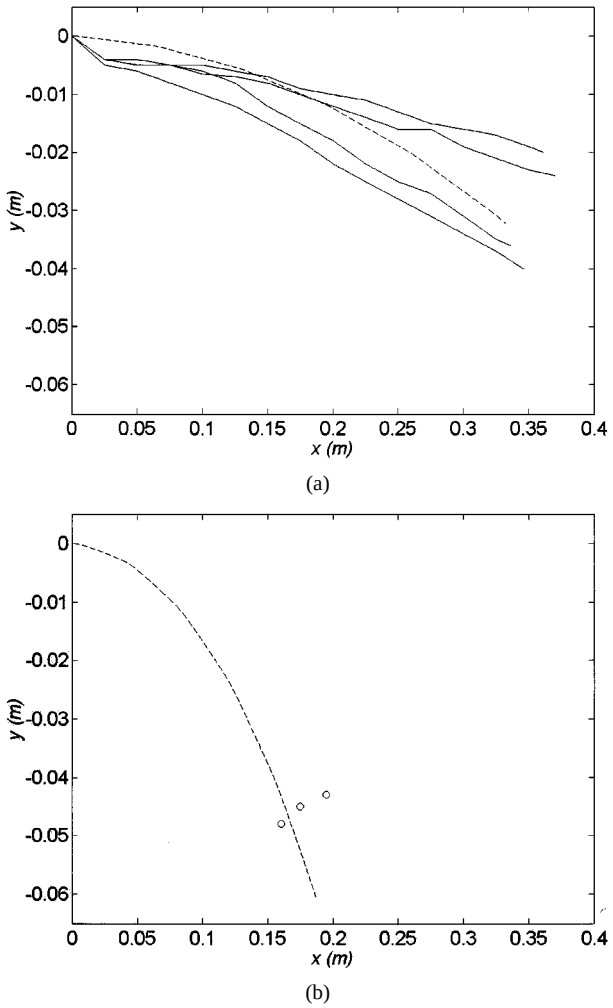

Fig. 10. (a) Improved simulated (dashed) and experimental (solid) results for paper motion surface. (b) Improved simulated (dashed) and experimental (O) results for carpet motion surface.

is implemented in simulation, and then compared with the existing experimental data. The improved friction model accounts for the rigid material in the discontinuities between wheel rollers (Fig. 5).

Fig. 9 show simulated results for the same motion input case as for Fig. 6; Fig. 9 includes the real-world effect of the rigid material between the wheel rollers. Again, to save space, the simulated results are shown only for the paper motion surface in Fig. 9. Fig. 9(a) shows the Cartesian displacements and Fig. 9(b) shows the associated sliding speeds v_{Wi} for each wheel, for the simulated pure X motion on the paper surface. Again in Fig. 9(b), the simulated sliding speeds for wheels one and two are identical due to symmetry. As seen in Fig. 9(b), slipping again is encountered at the start and end of motion. In addition, wheel three experiences significant slip during the middle of the motion; this behavior was not predicted by the initial friction model. The effect, seen in Fig. 9(a), is that x falls short of its goal of 0.4 m by 53 mm, while y drifts -22 mm from the desired zero. ϕ drifts from its commanded value of zero by -0.111 rad in the worst case at the end. All three Cartesian drifts are much larger than predicted in Fig. 6(a).

Fig. 10(a) and (b) compare the preceding experimental data with this new, improved friction model simulation, plotting y versus x for paper and carpet motion surfaces, respectively. The experimental data of Fig. 10 is identical to that of Fig. 7.

In Fig. 10(a), the dashed curve is the simulated result using the improved friction model and the paper motion surface; this curve was obtained by plotting y versus x from Fig. 9(a). The four solid curves are the previously-presented experimental results for the same motion case, with the paper motion surface. The three single **O** points in Fig. 9(b) are the same experimental ending points with the carpet motion surface as shown in Fig. 7(b). The dashed curve is the simulated result using the improved friction model and the carpet motion surface (not previously shown). Clearly, the simulation/experimental agreement obtained by the improved friction model [shown in Fig. 10(a) and (b)] is much better than that displayed in Fig. 7(a) and (b) which used the initial friction model.

Figs. 7 and 10 ignore the mobile robot orientation ϕ. For the paper motion surface, the simulated (improved friction model) ending value of ϕ is -0.111 rad. No experimental data are available for this case, since the four experimental trials all ended with very small ϕ, close to the angular measurement precision. Even so, the agreement is good qualitatively since the simulated ending angle is also small. For the carpet motion surface, the simulated ending value of ϕ is 0.558 rad, which compares favorably with the measured experimental values of 0.524, 0.506, and 0.489 rad [left-to-right for the experimental **O**s of Fig. 10(b)].

As mentioned earlier, we assumed the dynamic friction coefficient is equal to the static friction coefficient. Perhaps better simulation/experimental agreement would be obtained by use of a combined friction coefficient model where the dynamic friction is less. This is difficult to measure, and we are satisfied with the agreement shown in Fig. 10, using static coefficients of friction only.

V. Conclusion

This paper has presented a dynamic model for omnidirectional wheeled mobile robots and vehicles, considering slipping between the wheels and motion surface. We derived the dynamics model, experimentally measured the friction coefficients, and validated our friction model by experimentally measuring the maximum force causing slip at various robot orientations. Simulation examples were presented to demonstrate slipping motion; the initial friction model results did not agree with experimental trajectory data. Therefore, an improved friction model was developed, considering the rigid material in the discontinuities between omnidirectional wheel rollers. With this improved friction model, the simulation agreed well with the experimental data. Two motion surfaces, paper and carpet, were used in simulation and experiments, with different friction properties. A pure X translational motion was commanded in simulation and experiment; simulations show that slipping for Y translational motions are not as severe, due to robot symmetry. With zero commanded rotational motion, the robot experienced undesirable slip in rotational motion. In the future, we will study slipping in commanded rotational motions.

During our initial modeling and experimental work, we thought that omnidirectional robot slip dynamics would be limited by high velocities and accelerations. This is still true, however, we learned that for our robot design, an equally

significant factor in slip dynamics is the rigid material between rollers, even at low motion rates and accelerations. Our development team response was to file away as much of that material as possible to avoid contact in these sectors (after the experiments). However, this paper is pertinent to any omnidirectional mobile robot design with or without discontinuity between rollers. Our work demonstrated reasonable simulation/experimental agreement and we feel that we have captured the slip dynamics behavior of our design. A future improvement is to use static and dynamic coefficients of friction. Due to our demonstrated agreement, we conclude that the static coefficients of friction are adequate. For different omnidirectional robot designs, our modeling and simulation work will apply, but significant experimental work is still required to measure the various friction coefficients, and to fully understand the dynamic slip behavior.

Since our objective was to model and understand the sliding dynamics problem, this paper does not focus on real-time control. We will develop real-time control in the future based on our dynamic model, including measurement of variables for feedback control to overcome slipping dynamics.

REFERENCES

[1] C. C. De Wit, "Trends in mobile robot and vehicle control," *Control Problems in Robotics and Automation* , pp. 151–175, 1998.

[2] J. Borenstein, H. R. Everett, and L. Feng, "Mobile robot positioning: Sensors and techniques," *J. Robot. Syst.*, vol. 14, pp. 231–249, 1997.

[3] B. J. Choi and S. V. Sreenivasan, "Gross motion characteristics of articulated mobile robots with pure rolling capability on smooth uneven surfaces," *IEEE Trans. Robot. Automat.*, vol. 15, pp. 340–343, Apr. 1999.

[4] A. Hamdy and E. Badreddin, "Dynamic modeling of a wheeled mobile robot for identification, navigation and control," in *Proc. IMACS Conf. Modeling and Control of Technol. Syst.*, 1992, pp. 119–128.

[5] R. Rajagopalan, "A generic kinematic formulation for wheeled mobile robots," *J. Robot. Syst.*, vol. 14, pp. 77–91, 1997.

[6] S. Shekhar, "Wheel rolling constraints and slip in mobile robots," in *Proc. IEEE Int. Conf. Robotics and Automation*, vol. 3, 1997, pp. 2601–2607.

[7] R. Balakrishna and A. Ghosal, "Modeling of slip for wheeled mobile robots," *IEEE Trans. Robot. Automat.*, vol. 11, pp. 126–132, Feb. 1995.

[8] S. Scheding, G. Dissanayake, E. M. Nebot, and H. Durrant-Whyte, "Experiment in autonomous navigation of an underground mining vehicle," *IEEE Trans. Robot. Automat.*, vol. 15, pp. 85–95, Feb. 1999.

[9] M.-J. Jung, H.-S. Kim, S. Kim, and J.-H. Kim, "omnidirectional mobile base OK-II," in *Proc. IEEE Int. Conf. Robotics and Automation*, vol. 4, 2000, pp. 3449–3454.

[10] K. L. Moore, M. Davidson, V. Bahl, S. Rich, and S. Jirgal, "Modeling and control of a six-wheeled autonomous robot," in *Proc. American Control Conf.*, vol. 3, 2000, pp. 1483–1490.

[11] K. Watanabe, Y. Shiraishi, S. Tzafestas, J. Tang, and T. Fukuda, "Feedback control of an omnidirectional autonomous platform for mobile service robots," *J. Intell. Robot. Syst.*, vol. 22, pp. 315–330, 1998.

[12] G. Witus, "Mobility potential of a robotic 6-wheeled omnidirectional drive vehicle (ODV) with Z-axis and tire inflation control," in *Proc. SPIE*, vol. 4024, 2000, pp. 106–114.

[13] S. Bhattacharya and S. Agrawal, "Spherical rolling robot: Design and motion planning studies," *IEEE Trans. Robot. Automat.*, vol. 16, pp. 835–839, Dec. 2000.

[14] Y. Mori, E. Nakano, T. Takahashi, and K. Takayama, "Mechanism and running modes of new omnidirectional vehicle ODV9," *JSME Int. J.*, ser. C, vol. 42, no. 1, pp. 210–217, 1999.

[15] S. L. Dickerson and B. D. Lapin, "Control of an omnidirectional robotic vehicle with mecanum wheels," in *Proc. Nat. Telesystems Conf.*, vol. 1, 1991, pp. 323–328.

[16] F. G. Pin and S. M. Killough, "A new family of omnidirectional and holonomic wheeled platforms for mobile robots," *IEEE Trans. Robot. Automat.*, vol. 10, pp. 480–489, Aug. 1994.

[17] F. Gustafsson, "Slip-based tire-road friction estimation," *Automatica*, vol. 33, no. 6, pp. 1087–1099, 1997.

[18] X. Claeys, J. Yi, L. Alvarez, R. Horowitz, and C. C. de Wit, "A dynamic tire/road friction model for 3D vehicle control and simulation," in *Proc. IEEE Intelligent Transportation Systems*, Oakland, CA, Aug. 25–29, 2001, pp. 483–488.

[19] H. Yong-Seob, L. Jihong, and T. C. Hsia, "A recursive dimension-growing method for computing robotic manipulability polytope," in *Proc. IEEE Int. Conf. Robotics and Automation*, 2000, pp. 2569–2574.

Robert L. Williams, II (M'97) received the Ph.D. degree from Virginia Polytechnic Institute and State University, Blacksburg, in 1988.

He was with the NASA Langley Research Center for five years, working in space telerobotic systems. He is currently an Associate Professor of Mechanical Engineering at Ohio University, Athens. His current research interests include the kinematics, dynamics, and control of mobile robots, parallel robots, cable-direct-driven robots, and haptic interfaces.

Brian E. Carter received the B.S. (*summa cum laude*) and M.S. degrees in mechanical engineering from Ohio University, Athens, in 1999 and 2001, respectively.

He is presently employed as a Mechanical Design Engineer at Automation Tooling Systems, Inc., Westerville, OH.

Mr. Carter was awarded the Dean's Scholarship and the Stocker Fund Scholarship by Ohio University.

Paolo Gallina received the Ph.D. degree from the University of Brescia, Brescia, Italy, in 1999.

He was with the University of Padova, Padova, Italy, as an Assistant Professor from 1999 to 2002. He was on leave as a Visiting Research Professor at Ohio University, Athens, in 2000–2001. He is currently an Associate Professor of Applied Mechanics and Vibrations in the Department of Energetics, University of Trieste, Trieste, Italy. His interests are vibrations, human–machine interfaces, and robotics, especially as applied to rehabilitation.

Giulio Rosati received the M.S. degree in mechanical engineering in 1999 from the University of Padova, Padova, Italy, where he is currently working toward the Ph.D. degree in applied mechanics at the Department of Innovation in Mechanics and Management.

His research interests are medical robotics and haptic interfaces.